



TECHNISCHE  
UNIVERSITÄT  
WIEN  
Vienna University of Technology

BACHELOR THESIS  
**ELECTRON VORTEX  
PROPAGATION IN  
AMORPHOUS SOLIDS**

LVA 133.010 ELEKTRONEN-ENERGIEVERLUSTSPEKTROMETRIE

STEFAN SACK

E1301753

JULY 2016

SUPERVISED BY:  
PROF. M. STÖGER-POLLACH  
DR. S. LÖFFLER AND DIPLO.-ING T. SCHACHINGER

## CONTENTS

1	Introduction	3
2	Vortex Solutions of the Schrödinger Equation	4
3	Creation of Vortexbeams	6
4	Multislice Method	7
5	Simulation of an Amorphous Solid	9
6	Vortex Propagation	12
7	Conclusion	19
8	Appendix	20

## LIST OF FIGURES

Figure 1	Vortex probability density . . . . .	6
Figure 2	Vortex mask . . . . .	7
Figure 3	Computation time of amorphous solid program . . . . .	10
Figure 4	Incident m=1 vortex and colorwheel . . . . .	12
Figure 5	Wavefunction at exit plane . . . . .	13
Figure 6	Probability density at exit plane . . . . .	13
Figure 7	$\langle \hat{L}_z \rangle$ in amorphous silicon . . . . .	14
Figure 8	$\langle \hat{L}_z \rangle$ in amorphous platinum and Fe <sub>80</sub> Si <sub>6</sub> B <sub>13</sub> C <sub>1</sub> alloy . . . . .	15
Figure 9	Absolute value of Fourier coefficients . . . . .	16
Figure 10	Intensities of different vortex orders in exit plane . . . . .	18
Figure 11	Bar chart of intensities for different vortex orders in exit plane	18
Figure 12	$\langle \hat{L}_z \rangle$ in amorphous Fe <sub>80</sub> Si <sub>6</sub> B <sub>13</sub> C <sub>1</sub> alloy with different convergent semi angles . . . . .	20
Figure 13	$\langle \hat{L}_z \rangle$ in vacuum . . . . .	20

## 1 INTRODUCTION

The propagation of electron vortices in crystals has already been studied in detail numerically [1] and analytically [2].

It has been shown that the phase front of the vortex is greatly perturbed by the atomic potentials in the solid. Additionally, the expectation value of the angular momentum  $\langle \hat{L}_z \rangle$ , is subject to large quasi-periodical change during propagation. This is caused by scattering of the wavefunction on the atom potentials.

However, no investigations for amorphous solids have been conducted yet. It was suggested by Prof. Peter Schattschneider that this might hold some interesting results.

Therefore, the subject of this work is to simulate the propagation of electron vortices in amorphous solids.

The first part of this work provides some theoretical background on electron vortices, their creation and propagation, including the derivation of the multislice equation, which is crucial for all computer based wavefunction propagation of fast electrons.

The middle section gives some insight on the program that was coded for simulating an amorphous solid and the last section discusses the results that were obtained.

The conclusion will give a summery of the obtained results and propose some possible further investigations.

## 2 VORTEX SOLUTIONS OF THE SCHRÖDINGER EQUATION

The Schrödinger equation is the fundamental equation for describing quantum mechanical behaviour:

$$\hat{H}\psi = E\psi \quad (1)$$

With the Hamiltonian for a free particle  $\hat{H} = \frac{\hat{p}^2}{2m_e}$  and the quantum mechanical momentum operator  $\hat{p} = \frac{\hbar}{i}\nabla$  the Schrödinger equation becomes:

$$-\frac{\hbar^2}{2m_e} \nabla^2 \psi = E\psi \quad (2)$$

For cylindrical coordinates one obtains:

$$-\frac{\hbar^2}{2m_e} \left[ \frac{\partial^2}{\partial r^2} + \frac{1}{r} \frac{\partial}{\partial r} + \frac{\partial^2}{r^2 \partial \phi^2} + \frac{\partial^2}{\partial z^2} \right] \psi = E\psi \quad (3)$$

Using separation of variables

$$\psi(r, \phi, z) = R(r)\Phi(\phi)Z(z) \quad (4)$$

the partial differential equation (3) is transformed to:

$$\frac{R''}{R} + \frac{1}{r} \frac{R'}{R} + \frac{1}{r^2} \frac{\Phi''}{\Phi} = -\frac{Z''}{Z} - \frac{2m_e E}{\hbar^2} \quad (5)$$

This is consistent with the fact that the commutator of  $\hat{L}_z$  and  $\hat{p}_z$  vanishes,  $[\hat{L}_z, \hat{p}_z] = 0$ . That implies that these operators have a common eigenbasis.

Since the right side only depends on  $z$  whereas the left side depends on  $r$  and  $\phi$ , the equation can only hold in general if both sides are a constant  $-\kappa^2$ .

Using the same argument for the left side, one obtains three uncoupled differential equations

$$\frac{Z''}{Z} = \kappa^2 - \frac{2m_e E}{\hbar^2} \quad (6)$$

$$\frac{\Phi''}{\Phi} = -m^2 \quad (7)$$

$$r^2 \frac{R''}{R} + r \frac{R'}{R} + \kappa^2 r^2 - m^2 = 0 \quad (8)$$

where  $\kappa$  and  $m$  are constant and  $\in \mathbb{R}$ . With  $k_z^2 = \frac{2m_e E}{\hbar^2} - \kappa^2$  one obtains a plane wave solution for the first equation

$$Z \propto e^{ik_z z} \quad (9)$$

which is the eigenfunction of the momentum operator  $\hat{p}_z$ . The solution implies the dispersion relation  $E = \frac{\hbar^2}{2m_e}(k_z^2 + k^2)$ .  $E > 0$  since we are dealing with a free particle. The solution for the second equation yields:

$$\Phi \propto e^{im\phi} \quad (10)$$

which is the eigenfunction of the angular momentum operator  $\hat{L}_z$  in cylindrical coordinates. To obtain an unambiguous wavefunction, we want invariance under a transformation  $\phi \rightarrow \phi + 2\pi$ . This can only be true if  $m \in \mathbb{Z}$ .

The radial equation yields:

$$r^2 R(r)'' + r R(r)' + (\kappa^2 r^2 - m^2) R(r) = 0 \quad (11)$$

Substituting  $x = \kappa r$ , we obtain the Bessel differential equation:

$$x^2 R''(x) + x R(x) + (x^2 - m^2) R(x) = 0 \quad (12)$$

With the general solution:

$$R(\kappa r) = c_1 J_m(\kappa r) + c_2 Y_m(\kappa r) \quad (13)$$

For  $r \rightarrow 0$  the second kind Bessel function  $Y_m$  diverges which implies that  $c_2 = 0$  and we obtain the general solution for the problem.

$$\psi \propto J_m(\kappa r) e^{i(k_z z + m\phi)} \quad (14)$$

$\kappa$ ,  $k_z$  and  $m$  are the quantum numbers of the solution. This was first shown by [3]. Modes with well defined OAM (orbital angular momentum) and momentum are called vortex beams  $\psi_m \propto e^{i(k_z z + m\phi)}$ . These vortex beams have some very interesting properties. First of all they carry quantised OAM.

$$\langle \hat{L}_z \rangle = \frac{\langle \psi | \hat{L}_z | \psi \rangle}{\langle \psi | \psi \rangle} = \hbar m \quad (15)$$

Where  $m \in \mathbb{Z}$ . For the probability  $\rho = |\psi|^2$  and current density  $\mathbf{j} = \frac{\hbar}{2m_e i} (\psi^* \nabla \psi - \psi \nabla \psi^*)$  of the vortex solution Eq. 14, we obtain:

$$\rho_m \propto |J_m(\kappa r)|^2 \quad \mathbf{j}_m(r) = \frac{\hbar}{m_e} \left( \frac{m}{r} \mathbf{e}_\phi + k_z \mathbf{e}_z \right) \rho_m \quad (16)$$

For  $m = 0$  the beam carries no OAM and the probability density has a maximum at  $r = 0$ , whereas for  $m \neq 0$  the probability density is zero at the center, see Fig. 1. Note that just like a plane wave, the wave function cannot be normalised  $\int_{\mathbb{R}} d^3r \rho_m \rightarrow \infty$ . This issue can be resolved by a suitable envelope or boundary condition that restricts the wave function on a finite interval.

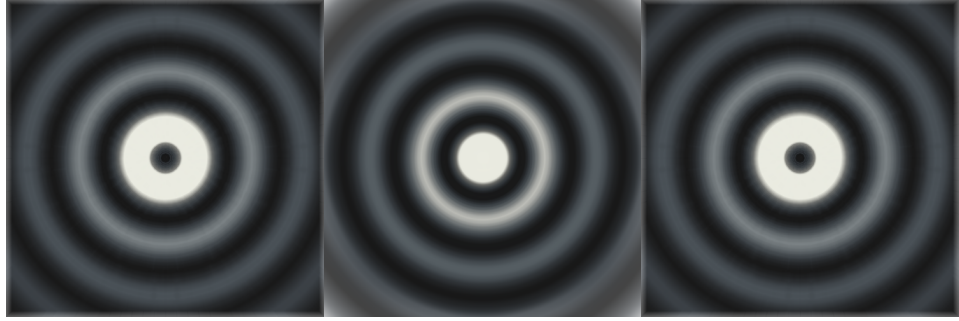


**Figure 1:** Vortex probability density  $\rho_m$  for  $m = -1$  (left),  $m = 0$  (center) and  $m = 1$  (right). White corresponds to a high probability density, whereas black corresponds to a low probability density.

### 3 CREATION OF VORTEXBEAMS

An important question to ask is how one can create such a vortex beam carrying angular momentum. We usually observe plane electron waves  $e^{ik_z z}$  carrying no angular momentum. Due to the conservation of angular momentum this means that for a system with no initial angular momentum, there can only be a composition of angular momentum that adds up to zero.

The idea is to send a plane wave onto some kind of mask that decomposes the wave into vortex beams carrying angular momentum that add up to zero in total. This means that if we just want one vortex beam carrying OAM the mask has to carry the opposite amount of OAM. Since any macroscopic object has a very large moment of inertia in comparison to an OAM of  $m\hbar$ , the OAM of the mask can be neglected.

One way of constructing vortex beams is to create an even number of vortex beams with opposite OAM, so that it adds up to zero. After passing through the mask, the electron is a free electron, which means that the wave function has to be the eigenfunction of the momentum operator  $\hat{p}_z$ . Hence, the wave function behind the mask is generally given by  $\psi = T e^{ik_z z}$ , where  $T$  is the transmission amplitude. We construct the transmission amplitude as a superposition of the desired vortex beam with an arbitrary plane wave orthogonal to the  $z$  direction.

$$T \propto |\psi_{\text{out}} + \psi_{\text{ref}}|^2 = |e^{im\phi} + e^{ik_x x}|^2 = 2(1 + \cos(m\phi - k_x x)) \quad (17)$$

Where  $k_x = \frac{2\pi}{d}$  with the lattice distance  $d$ . The exit wave function is therefore

$$\begin{aligned} \psi &= T e^{ik_z z} \\ &= 2 \exp(ik_z z) + \exp(im\phi + i(k_z z + k_x x)) + \exp(-m\phi + i(k_z z - k_x x)). \end{aligned} \quad (18)$$

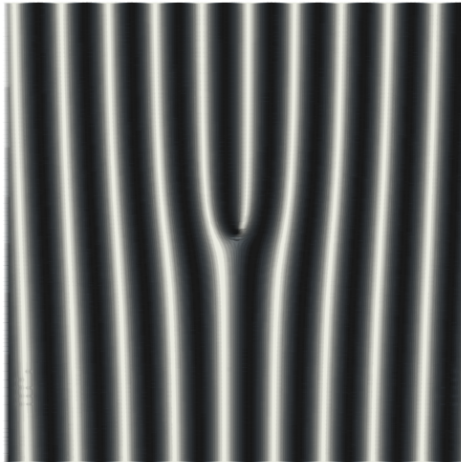


**Figure 2:** Contour plot of a vortex mask. White and black correspond to high and low thickness respectively.

The first term is a plane wave without OAM, whereas the second and third term are vortex beams propagating under the angle  $\pm \arctan(k_x/k_z)$  with opposite OAM [3].

The transmission amplitude  $T$  is the amplitude of the exit wave, so it must be proportional to the thickness of the mask. A contour plot of the vortex mask is shown in Fig. 2. This means that one can create vortex beams by sending a plane wave on a mask which has a varying thickness just like in Eq. 17. The making of such a mask would be a tedious process and it would block most of the intensity. That is why a discretisation given by

$$T = \begin{cases} 1, & \text{if } T \geq 2 \\ 0, & \text{else} \end{cases} \quad (19)$$

is usually used. The discretisation of the mask can be understood as a superposition of reference waves  $\psi_{\text{ref}}$  with different wavenumbers  $k_x$ . Therefore higher vortex orders than  $m = \pm 1$  appear in the exit wave.

## 4 MULTISLICE METHOD

This section discusses how the propagation of a wave package through a specimen can be calculated using the multislice method [4].

As the electron enters the specimen, it is scattered multiple times on its path. The main source for scattering is given by the electrostatic potential  $V(x, y, z)$  caused by the atoms. So the eigenfunction has to be calculated for a Hamiltonian that includes

the potential energy.

$$\left[ -\frac{\hbar^2}{2m_e} \nabla^2 - eV(x, y, z) \right] \psi_f(x, y, z) = E\psi_f(x, y, z) \quad (20)$$

The electron motion will mainly be in the  $z$  direction, so we can make the ansatz that  $\psi_f$  is a product of a wave moving in  $z$  direction and a small factor caused by the scattering.

$$\psi_f(x, y, z) = \psi(x, y, z)e^{i2\pi z/\lambda} \quad (21)$$

With the electron wavelength  $\lambda$ . We are only dealing with elastic scattering, so the total energy of the electron can be expressed by  $E = \hbar^2/2m_e\lambda^2$ , see [4] for reference. Insertion of Eq. 21 in Eq. 20 and dropping the factor  $\exp(2\pi iz/\lambda)$  yields:

$$-\frac{\hbar^2}{2m} \left[ \nabla_{xy}^2 + \frac{\partial^2}{\partial z^2} + \frac{4\pi i}{\lambda} \frac{\partial}{\partial z} + \frac{2m_e e V(x, y, z)}{\hbar^2} \right] \psi(x, y, z) = 0 \quad (22)$$

Seeing that the motion of the electron is predominately in the  $z$  direction, any change of  $\psi$  in the  $z$  direction will be relatively small. So we can estimate that

$$\left| \frac{\partial^2 \psi}{\partial z^2} \right| \ll \left| \frac{1}{\lambda} \frac{\partial \psi}{\partial z} \right|. \quad (23)$$

Using Eq. 23 and  $\sigma = 2\pi m_e e \lambda / \hbar^2$ , which can be understood as an interaction parameter, the Schrödinger Eq. 20 for fast electrons traveling in the  $z$  direction can be approximated to:

$$\frac{\partial \psi(x, y, z)}{\partial z} = \left[ \frac{i\lambda}{4\pi} \nabla_{xy}^2 + i\sigma V(x, y, z) \right] \psi(x, y, z) \quad (24)$$

Offsetting the initial value to  $z$  and integrating to  $z + \Delta z$  yields:

$$\psi(x, y, z + \Delta z) = \exp \left[ \frac{i\lambda}{4\pi} \Delta z \nabla_{xy}^2 + i\sigma \int_z^{z+\Delta z} V(x, y, z') dz' \right] \psi(x, y, z) \quad (25)$$

Using the Zassenhaus theorem [5], Eq. 25 can be further simplified.

$$\begin{aligned} \psi(x, y, z + \Delta z) &\approx \exp \left( \frac{i\lambda \Delta z}{4\pi} \nabla_{xy}^2 \right) t(x, y, z) \psi(x, y, z) \\ t(x, y, z) &= \exp \left[ i\sigma \int_z^{z+\Delta z} V(x, y, z') dz' \right] = \exp \left[ i\sigma v_{\Delta z}(x, y, z) \right] \end{aligned} \quad (26)$$

$t(x, y, z)$  is the transmission function and  $v_{\Delta z}(x, y, z)$  is the projected potential [4]. According to Kirkland [4],  $\exp\left(\frac{i\lambda\Delta z}{4\pi}\nabla_{xy}^2\right)$  may be interpreted as:

$$\exp\left(\frac{i\lambda\Delta z}{4\pi}\nabla_{xy}^2\right) = p(x, y, \Delta z) \otimes \quad (27)$$

where  $\otimes$  is a two dimensional convolution (in  $x$  and  $y$ ) and  $p(x, y, \Delta z)$  is the propagator function in real space for a distance  $\Delta z$ :

$$\begin{aligned} P(k, \Delta z) &= \exp(-i\pi\lambda k^2 \Delta z) \\ p(x, y, \Delta z) &= \text{FT}^{-1}[P(k, \Delta z)] = \frac{1}{i\lambda\Delta z} \exp\left[\frac{1}{i\lambda\Delta z}(x^2 + y^2)\right] \end{aligned} \quad (28)$$

If the specimen is now discretised in the  $z$ -direction and the slices are labeled  $n = 0, 1, 2, \dots$  then the combination of the above expressions gives the multislice Eq. 29:

$$\psi_{n+1}(x, y) = p_n(x, y, \Delta z_n) \otimes [t_n(x, y)\psi_n(x, y)] \quad (29)$$

The propagation of a given initial wave function  $\psi_0(x, y)$  can now be calculated numerically, using the multislice Eq. 29. The convolution can be efficiently calculated using the Fast Fourier Transformation. Eq. 29 can therefore be written as:

$$\psi_{n+1}(x, y) = \text{FT}^{-1}\{P_n(k_x, k_y, \Delta z_n)\text{FT}[t_n(x, y)\psi_n(x, y)]\} \quad (30)$$

To propagate a wave function, the specimen must be discretised in slices. The atom positions in each slice are projected to give the projected potential  $v_n(x, y)$ . The projected potential can then be used to calculate the transmission function  $t_n(x, y)$ . Eq. 30 can now be used to calculate the wave function in the  $(n + 1)^{\text{th}}$  slice.

Input data is therefore the initial wavefunction  $\psi_0(x, y)$  and the atom positions in each slice. For every crystal, a periodic slice stacking sequence can be found, representing the translation symmetry. This is not true in an amorphous solid. Atom positions are completely random and no translation symmetry exists.

## 5 SIMULATION OF AN AMORPHOUS SOLID

The propagation of a vortex through a crystal structure has already been studied in detail using the multi slice method, as described in the previous chapter. See [1] and [2] for details.

However, no investigations for amorphous solids were conducted.

It has been suggested by Prof. Peter Schattschneider that this might hold some interesting results.

Therefore, the task was to study vortex propagation in amorphous solids. As part of this work, a C/C++ program was written that can construct a suitable configuration file of an amorphous solid to use for the propagation. The program was implemented into an already existing workframe for vortex propagation by Dr. Stefan Löffler, which is based on the original multislice code from Kirkland [4].

The workframe allows to choose different initial vortex orders to propagate through the specimen, while the specimen is characterised by the atom positions in the slices. The propagated wave can be analysed in detail, ranging from phase to absolute square, expectation value of the angular momentum  $\langle \hat{L}_z \rangle$  and many more options.

A C/C++ script was written which calculates random atom positions and arranges the positions in the appropriate slice according to the position in the z direction.

Firstly, atom positions are randomly initialised, then the distance to every previous atom is checked. If the distance is lower than the sum of the covalent radii of both atoms, a new random position is assigned. This means that the atoms are idealised as hard spheres which have to fit into a given volume.

The computation time for this algorithm scales quadratically with the number of atoms (Fig. 3).

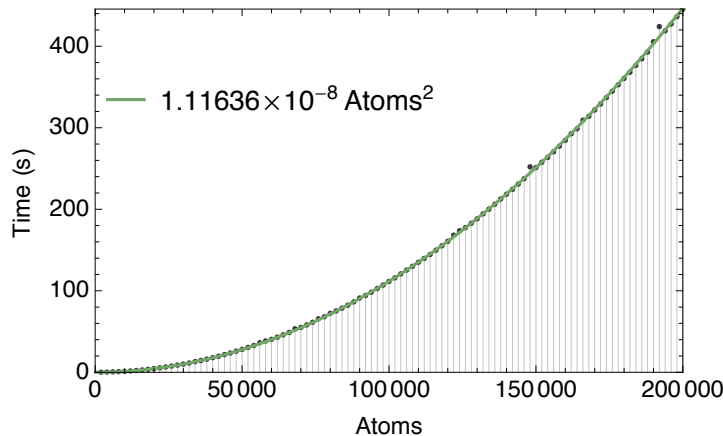


**Figure 3:** Computation time of the positioning algorithm for different numbers of atoms. Gray dots represent measured time, while the green line represents the fitting function.

Once all atom positions are calculated, they are arranged into the right slice, depending on the z position. Every slice contains a number of different elements with the associated atom positions. The final data is written into a configuration file, containing all necessary information for the vortex propagation.

All input data for the amorphous solid program is read from a configuration file. An example of a configuration file for Fe<sub>80</sub>Si<sub>6</sub>B<sub>13</sub>C<sub>1</sub> is provided:

```

density = 3e22;          #in Atoms/cm^3
size_x = 100;            #in Angstrom
size_y = 100;            #in Angstrom
size_z = 1000;           #in Angstrom
slice = 2;               #in Angstrom
dim = [2048,2048];      #in Pixels
seed = 0;                #optional

composition = (
{
    Z = 26;
    name = "Fe";
    fraction = 80;
},
{
    Z = 14;
    name = "Si";
    fraction = 6;
},
{
    Z = 5;
    name = "B";
    fraction = 13;
},
{
    Z = 6;
    name = "C";
    fraction = 1;
}
);

```

The configuration file has to include the particle density of the specimen, the specimen size in x-, y- and z-direction and the slice thickness. Furthermore, the dimension in pixels of the simulated area has to be provided, which is used by the main propagation program. The dimensions and slice thickness determine the precision of the simulation. A smaller slice thickness reduces the fundamental error introduced by the multislice approximation [4] at the cost of longer computation times and possibly larger numerical errors. The dimensions determine the number of pixels representing the x-, y-size of the specimen.

The option seed gives a starting value for the random number generator used by the computer. Since the random numbers generated by the computer are not really random, but follow a pattern, this opens the possibility to reproduce the exact same atom positions from a previous simulation at a later time. If no seed is provided in the configuration file, an arbitrary number will be used as a starting value.

The composition has to include the atomic number, name and fraction of the elements that are used. Fraction can either be provided in number of atoms or percentage.

Some additional information is provided in the command line once the program is started. Most notably the number of atoms, number of slices and volume packing ratio which is given by

$$\frac{\sum V_{\text{atoms}}}{V_{\text{total}}}.$$
 (31)

The ideal packing ratio for the simulation seems to be at 20-25%, which offers low computation times for a fairly realistic particle density.

For a high particle density, the algorithm might not find fitting atom positions inside

the volume. For that reason, the algorithm will try to find a fitting atom position only for a finite number of tries. This number is introduced as 10 times the number of atoms. The factor can be changed in the configuration file.

## 6 VORTEX PROPAGATION

Once the atom position configuration file is created, the vortex can be propagated through the specimen. A  $m = 1$  incident vortex was used and propagated at an energy of  $v_0 = 200\text{ kV}$  with a convergence semi angle of  $20\text{ mrad}$ . All further simulations were implemented for an area of  $(100\text{\AA})^2$  and a depth of  $1000\text{\AA}$ .

The incident  $m = 1$  vortex, Fig. 4, is not an eigenfunction of the vacuum Hamiltonian. This implies that the wavefunction will change during propagation through vacuum, Fig. 5 (a).

However, the characteristic phase factor  $|\psi_m\rangle = e^{im\phi}$ , which is the eigenfunction of the angular momentum operator  $\hat{L}_z$ ,

$$\hat{L}_z |\psi_m\rangle = \hbar m |\psi_m\rangle \quad (32)$$

is preserved. This also holds true for the time evolution of the incident wavefunction, since  $[\hat{L}_z, \hat{H}] = 0$  (in vaccum):

$$\hat{L}_z e^{i\hat{H}t} |\psi_m\rangle = e^{i\hat{H}t} \hat{L}_z |\psi_m\rangle = \hbar m e^{i\hat{H}t} |\psi_m\rangle \quad (33)$$

The only change is in the radial factor  $f_m(r, z)$  of the vortex,

$$\psi_m(r, z, \phi) = f_m(r, z) e^{im\phi} \quad (34)$$

which can be seen in Fig. 5 (a).

However, this is no longer true in a solid. The atom potentials cause scattering, which introduces different vortex orders. Thus, the wavefunction has to be expanded in terms of phase factors  $e^{im\phi}$ .

$$\psi(r, z, \phi) = \sum_{m=-\infty}^{\infty} f_m(r, z) e^{im\phi} \quad (35)$$

Fig. 5 (b) shows the wavefunction in the exit plane of amorphous silicon. The random scattering has caused some turbulence in the phase, but the corkscrew-like phase front can still be observed. Fig. 5 (c) shows the wavefunction in the exit plane of amorphous platinum. The stronger electrostatic potential of platinum causes further turbulences in the phase front.

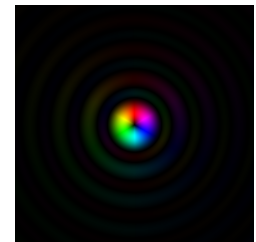
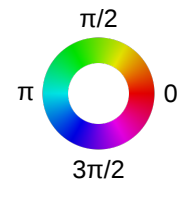


**Figure 4:** Phase of the incident wavefunction of  $m=1$  vortex with a convergence semi angle of  $2.06\text{ mrad}$  and color-wheel for reference of phase coloring. The phase image represents an area of  $(100\text{\AA})^2$ .

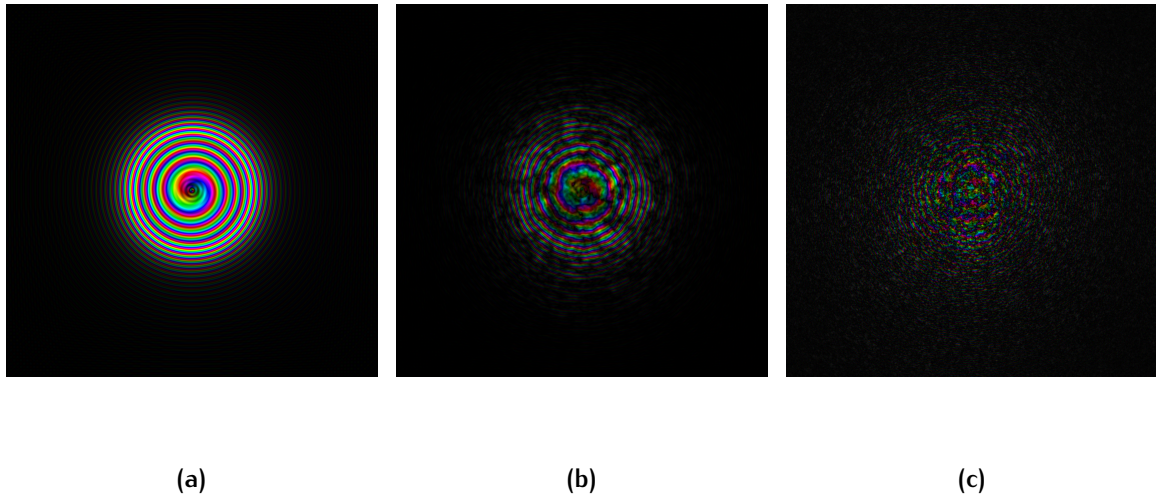


**Figure 5:** Wavefunction of  $m = 1$  vortex at the exit plane ( $1000\text{\AA}$ ), in vacuum (a), amorphous silicon with a particle density of  $4 \times 10^{22} \text{ atoms/cm}^3$  (b) and amorphous platinum with a particle density of  $2.5 \times 10^{22} \text{ atoms/cm}^3$  (c). An area of  $(100\text{\AA})^2$  was used for the simulation. Note the color wheel in Fig. 4 for phase coloring reference. A convergence semi angle of 20mrad was used.

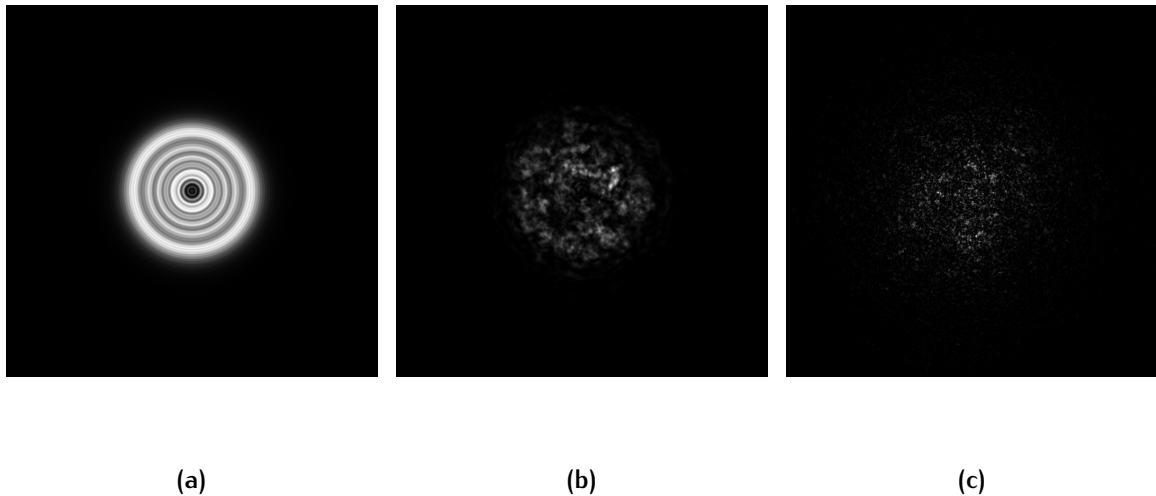


**Figure 6:** Probability density at the exit plane ( $1000\text{\AA}$ ), in vacuum (a), amorphous silicon with a particle density of  $4 \times 10^{22} \text{ atoms/cm}^3$  (b) and amorphous platinum with a particle density of  $2.5 \times 10^{22} \text{ atoms/cm}^3$  (c). An area of  $(100\text{\AA})^2$  was used for the simulation. A convergence semi angle of 20 mrad was used. Black corresponds to low probability density, whereas white corresponds to high probability density.

A detailed analysis has been conducted numerically [1] and analytically [2] for crystals. As shown in [1] the positioning of the vortex in relation to an atom column plays a crucial role for the evolution of the wavefunction. In an amorphous solid however, the atoms are positioned randomly, so that this no longer holds true.

The probability density for all three cases is shown in Fig. 6. The enhanced scattering in platinum can also be seen in Fig. 6 (c) when compared to silicon in Fig. 6 (b). Transmitted electrons appear to be randomly positioned in the exit plane of the amorphous solids, Fig. 6 (b) and (c).

As shown in [1] and [2], the expectation value  $\langle \hat{L}_z \rangle$  of the angular momentum is changing greatly as a function of penetration depth for a crystal. This is explained by the fact that the crystal Hamiltonian no longer commutes with the angular momentum operator due to the added potential in the crystal Hamilton operator,  $\hat{H}_{\text{solid}} = -\frac{\hat{p}^2}{2m} + \hat{V}$ .

$$[\hat{L}_z, \hat{H}_{\text{solid}}] = -\frac{1}{2m} [\hat{L}_z, \hat{p}^2] + [\hat{L}_z, \hat{V}] \quad (36)$$

Since  $[\hat{L}_z, \hat{p}^2] = 0$ ,

$$[\hat{L}_z, \hat{H}_{\text{solid}}] = [\hat{L}_z, \hat{V}] \neq 0 \quad (37)$$

However, as the simulation shows, this is not true for amorphous solids. Scattering gives rise to different vortex orders, as discussed at a later point, but the expectation value  $\langle \hat{L}_z \rangle$  of the angular momentum remains relatively stable about the initial value.

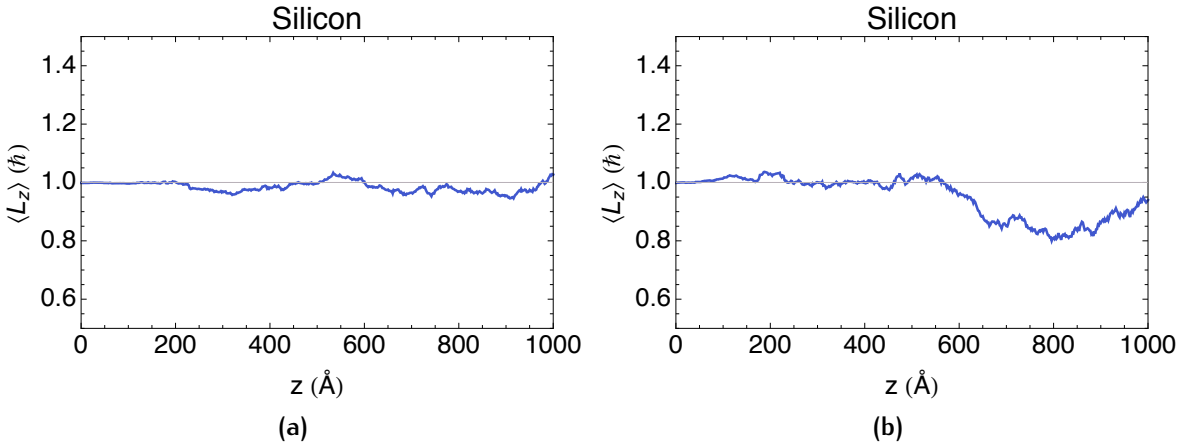


**Figure 7:** Expectation value  $\langle \hat{L}_z \rangle$  for  $m = 1$  vortex as a function of penetration depth for amorphous silicon with a particle density of  $2.5 \times 10^{22} \text{ atoms/cm}^3$  (a) and  $4 \times 10^{22} \text{ atoms/cm}^3$  (b). A convergence semi angle of 20 mrad was used.

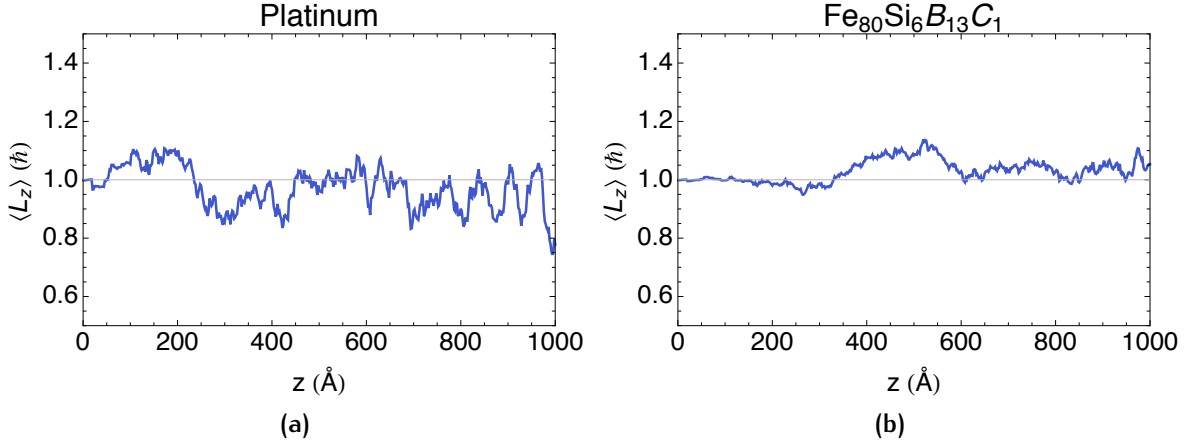


**Figure 8:** Expectation value  $\langle \hat{L}_z \rangle$  as a function of penetration depth for amorphous platinum with a particle density of  $2.5 \times 10^{22} \text{ atoms/cm}^3$  (a) and an  $\text{Fe}_{80}\text{Si}_6\text{B}_{13}\text{C}_1$  alloy with a particle density of  $3 \times 10^{22} \text{ atoms/cm}^3$  (b). Due to its magnetic character, the  $\text{Fe}_{80}\text{Si}_6\text{B}_{13}\text{C}_1$  alloy is currently under active investigation for EMCD.

This can be seen in Fig. 7 and Fig. 8. A higher particle density, as seen in Fig. 7 (b), causes more scattering, whereby  $\langle \hat{L}_z \rangle$  fluctuates more when compared to a lower particle density, as seen in Fig. 7 (a).

A high atomic number corresponds to a strong electrostatic potential, which enhances scattering and change of  $\langle \hat{L}_z \rangle$ . This can be seen for platinum, Fig. 8 (a) and an  $\text{Fe}_{80}\text{Si}_6\text{B}_{13}\text{C}_1$  alloy, Fig. 8 (b).

This can be explained by the fact that since  $[\hat{L}_z, \hat{p}^2] = 0$ , the Hamiltonian and angular momentum operator only span a common eigenbasis if:

$$[\hat{L}_z, \hat{V}] \cong \frac{\partial \hat{V}}{\partial \phi} = 0 \quad (38)$$

This means that the expectation value of the angular momentum  $\langle \hat{L}_z \rangle$  is preserved. On average this holds true in an amorphous solid, because the vortex sees a mean potential which is on average angular symmetric. This is trivially satisfied in vacuum, see Fig. 13 in the appendix.

Eq. 9 is also known as a complex Fourier series with the complex Fourier coefficients  $f_m(r)$ . The Fourier coefficients were calculated in Mathematica and the absolute value  $|f_m(r)|$  was plotted as a function of radius and penetration depth in Fig. 9 for silicon with a  $m = 1$  vortex.

Due to scattering they change as a function of the penetration depth. Fig. 9 shows that the change is along the convergence semi angle of the incident wavefunction. The further the vortex enters into the solid, the more pronounced Fourier coefficients different to the incident coefficient  $f_1(r)$  become.

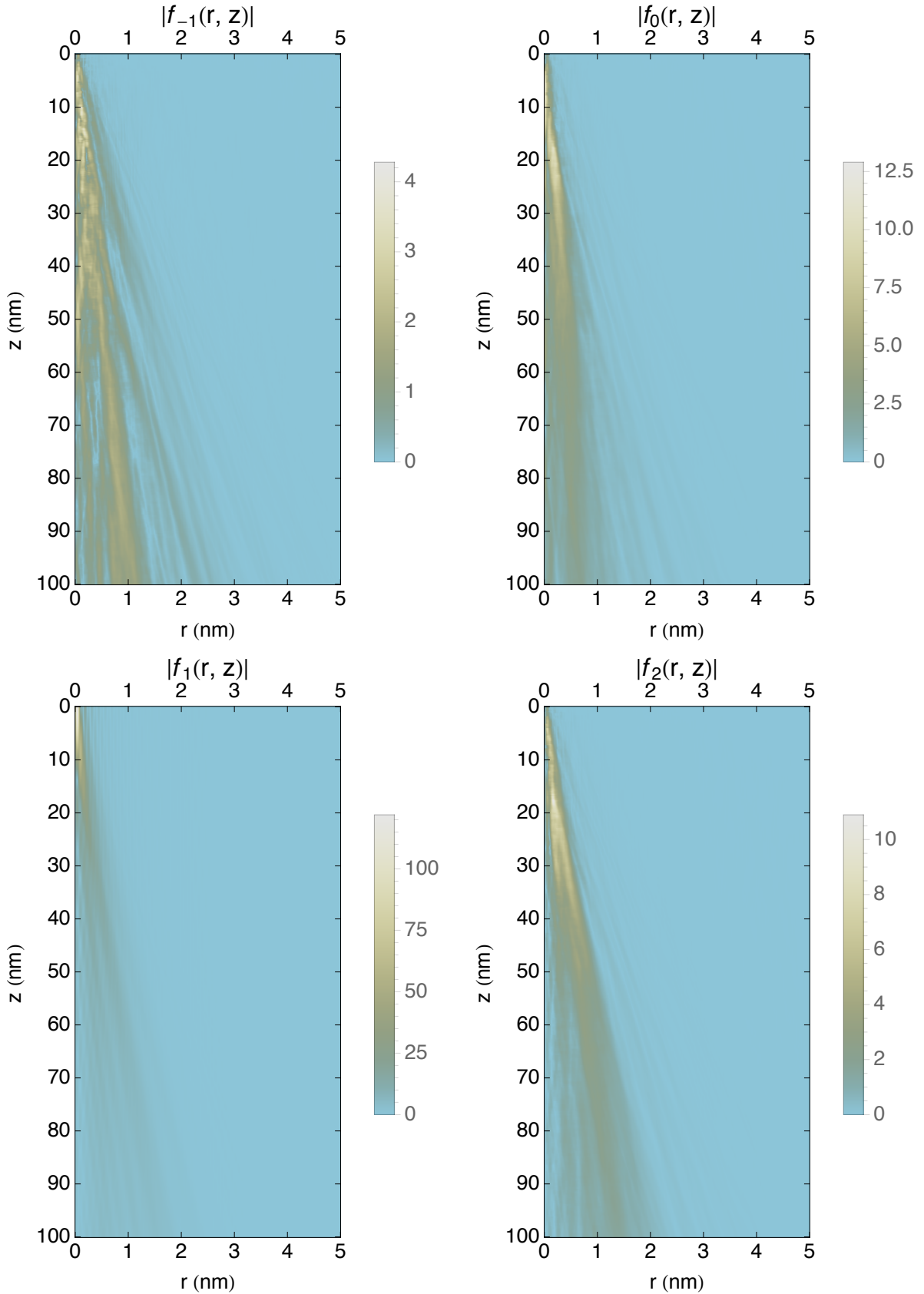


**Figure 9:** Absolute value of Fourier coefficients  $|f_m(r, z)|$  as a function of radius and penetration depth in amorphous silicon with a particle density of  $4 \times 10^{22} \text{ atoms/cm}^3$  for a  $m = 1$  vortex. A convergence semi angle of 20mrad and an area of  $(100\text{\AA})^2$  was used in the simulation.

The total intensity of the wavefunction for a given penetration depth is given by:

$$I(z) = |\psi(r, z, \phi)|^2 = \int \psi(r, z, \phi)^* \psi(r, z, \phi) r dr d\phi \quad (39)$$

Since the wavefunction in this case is not normalised, this is an arbitrary real value. Insertion of the Fourier expansion (Eq. 9) and changing the order of sum and integration yields:

$$\sum_{m,m'} \int f_{m'}(r, z)^* f_m(r, z) e^{i(m-m')\phi} dr d\phi := \sum_{m=-\infty}^{\infty} \int |f_m(r, z)|^2 r dr := \sum_{m=-\infty}^{\infty} I_m(z) \quad (40)$$

$I_m(z)$  represents the intensity of each vortex order as a function of penetration depth. Due to scattering, the intensity of the incident  $m = 1$  vortex  $I_1(z)$  decreases as a function of the penetration depth, while intensities of different orders increase. This can be seen in Fig. 10 and Fig. 11.

The intensities of the vortex orders next to the incident  $m = 1$  vortex, namely  $m = 0$  and  $m = 2$  increase significantly at around  $15\text{nm}$  and reach saturation at an intensity of about 0.055. This can be seen in Fig. 10.

The further a vortex order is away from the incident  $m = 1$ , the slower the increase in intensity, as seen in Fig. 10 and Fig. 11.

The intensity of the incident  $m = 1$  vortex seems to decrease linearly with the penetration depth, Fig. 10, while the total intensity remains the same. Fig. 11 hints at a slight asymmetry in increase of intensity for vortex orders  $m = 0$  and  $m = 2$ . From a mathematical point of view, there is no reason for an amplified increase of the  $m = 2$  vortex intensity. This phenomena might be caused by random fluctuation, but further investigation is needed to answer this question sufficiently.

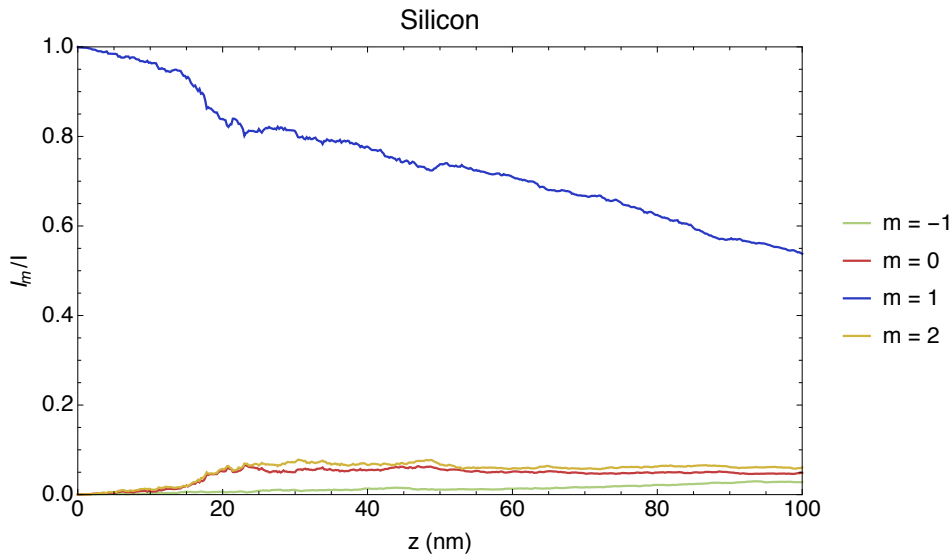


**Figure 10:** Vortex intensities for  $m = 1$  vortex in silicon with a particle density of  $4 \times 10^{22} \text{ atoms/cm}^3$  as a function of penetration depth. A convergence semi angle of 20mrad was used.

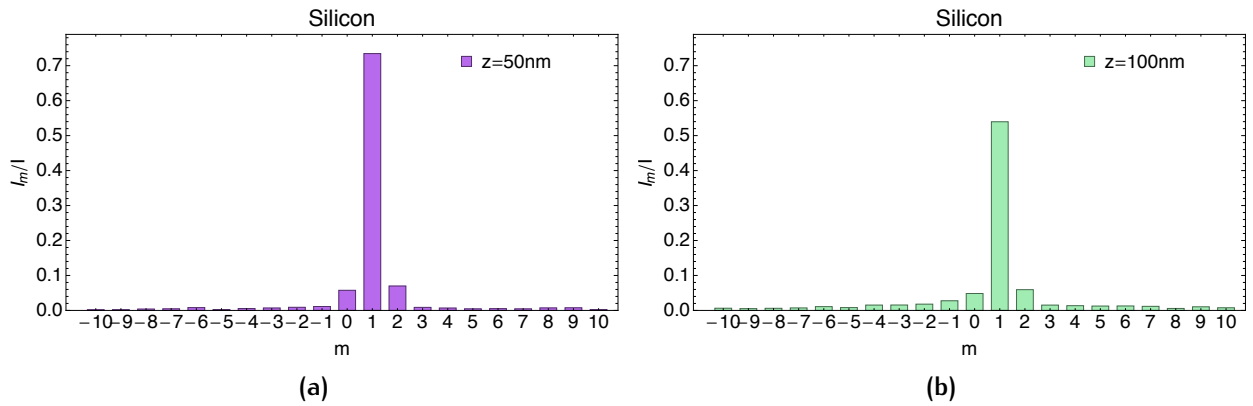


**Figure 11:** Vortex intensities after 50nm (a) and 100nm (b) propagation in amorphous silicon. A  $m=1$  vortex was used for propagation in amorphous silicon with a particle density of  $4 \times 10^{22} \text{ atoms/cm}^3$ . A convergence semi angle of 20mrad was used.

## 7 CONCLUSION

In the course of this work, a theoretical background about vortex solutions of the Schrödinger equation has been established and electron vortex creation as well as propagation was discussed briefly, with an emphasis on theory. See section 1-4. The main subject of this work was to study the propagation of electron vortices in amorphous solids. Therefore, a C/C++ program was written, which creates a suitable configuration file of an amorphous solid. The created configuration file was used in an existing work frame for vortex propagation (section 5).

The behaviour of the expectation value of the angular momentum as a function of penetration depth has been of special interest in the analysis. The data shows that unlike in a crystal, the expectation value of the angular momentum remains stable about the initial value during propagation, see Fig. 7 and 8.

This was explained by the fact that due to the random distribution of atoms in an amorphous solid, the angular momentum operator commutes with the atom potential operator on average. See Eq. 38 . This certainly does not hold true at every point during the propagation, which explains the fluctuation of the expectation value of the angular momentum. Scattering of the wavefunction on the atom potentials introduces new vortex orders. Hence, the wavefunction at the exit plane has to be constructed as a superposition of different vortex orders. This expansion is known as a complex Fourier series. The Fourier coefficients were calculated via Mathematica and analysed as a function of radius and penetration depth.

Further investigation of the intensities of all vortex orders has shown that the intensity of the incident vortex decreases, while the intensities of other vortex orders increase (Fig. 10). The neighbouring vortex orders of the incident vortex order show the most increase in intensity.

There is a hint on a slight asymmetry in terms of increase in intensity, of vortex orders neighbouring the incident vortex order (Fig. 11). This might just be a random fluctuation or caused by a phenomena that has not been considered yet. Further investigation is needed to answer this question.

Finally, I would like to thank Dr. Stefan Löffler and Dipl.-Ing. Thomas Schachinger for their assistance and helpful input during the course of this work.

## 8 APPENDIX

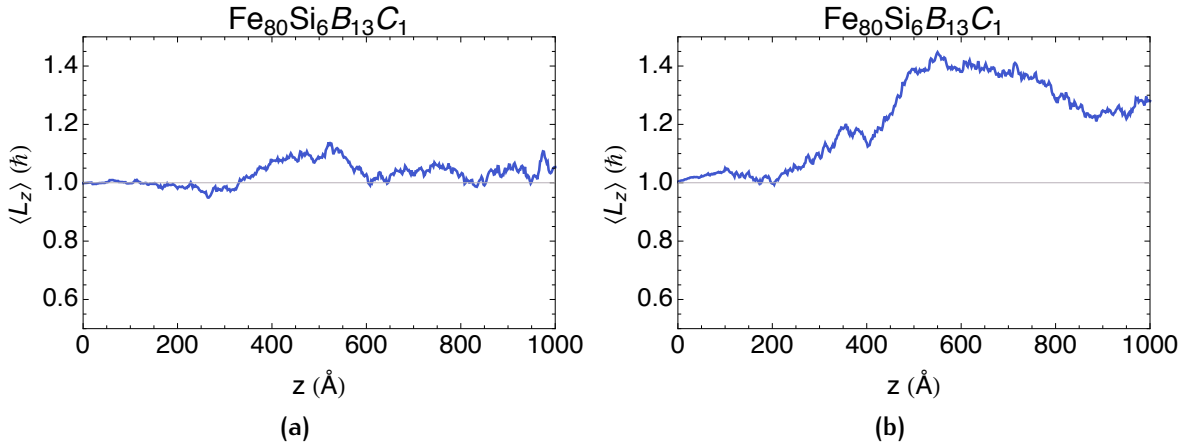


**Figure 12:** Expectation value  $\langle \hat{L}_z \rangle$  of  $m=1$  vortex as a function of penetration depth for an amorphous  $\text{Fe}_{80}\text{Si}_6\text{B}_{13}\text{C}_1$  alloy with a particle density of  $3 \times 10^{22} \text{ atoms/cm}^3$ . A convergence semi angle of  $20\text{mrad}$  (a) and  $2.06\text{mrad}$  (b) was used.

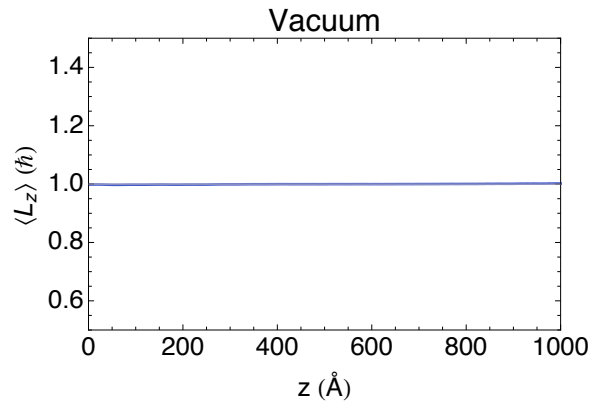


**Figure 13:** Expectation value  $\langle \hat{L}_z \rangle$  for  $m = 1$  vortex as a function of penetration depth in vacuum. A convergence semi angle of  $20\text{mrad}$  was used. The expectation value  $\langle \hat{L}_z \rangle$  remains at the incident value, which is to be expected in vacuum. The simulation nicely matches the theory.

## REFERENCES

- [1] Stefan Löffler and Peter Schattschneider. *Elastic propagation of fast electron vortices through crystals*. Acta Crystallographica, 2012.
- [2] Huolin L. Xin and Haimei Zheng. *On-column 2p bound state with topological charge  $\pm 1$  excited by an atomic-size vortex beam in an aberration-corrected scanning transmission electron microscope*. Acta Cryst., 1974.
- [3] P. Schattschneider and J. Verbeeck. *Theory of free electron vortices*. Ultramicroscopy, 2011.
- [4] Earl J. Kirkland. *Advanced Computing in Electron Microscopy*. Plenum Press, 1998.
- [5] P. Goodman and A.F. Moodie. *Numerical evaluation of N-beam wave functions in electron scattering by the multislice method*. Acta Cryst., 1974.